INTERNATIONAL JOURNAL FOR NUMERICAL METHODS IN FLUIDS, VOL. 9, 943–962 (1989)

NAVIER–STOKES COMPUTATION OF TRANSONIC VORTICES OVER A ROUND LEADING EDGE DELTA WING

BERNHARD MÜLLER*

FFA, The Aeronautical Research Institute of Sweden, S-161 11 Bromma, Sweden

AND

ARTHUR RIZZI

FFA, The Aeronautical Research Institute of Sweden, S-161 11 Bromma, Sweden, and KTH, The Royal Institute of Technology, S-100 44 Stockholm, Sweden

SUMMARY

A 3D Navier–Stokes solver has been developed to simulate laminar compressible flow over quadrilateral wings. The finite volume technique is employed for spatial discretization with a novel variant for the viscous fluxes. An explicit three-stage Runge–Kutta scheme is used for time integration, taking local time steps according to the linear stability condition derived for application to the Navier–Stokes equations. The code is applied to compute primary and secondary separation vortices at transonic speeds over a 65° swept delta wing with round leading edges and cropped tips. The results are compared with experimental data and Euler solutions, and Reynolds number effects are investigated.

KEY WORDS Navier–Stokes solver Vortex motion Finite volume method Viscous flow Delta wing

1. INTRODUCTION

Even at moderate angles of attack, the flow over a swept delta wing is characterized by a pair of symmetric primary vortices separating on the leeward side from the leading edges and symmetric counter-rotating secondary vortices separating from the leeward side inboard of the leading edges.[1]

Since the augmented lift induced by the leeside vortices is of great aerodynamic usefulness, a number of experimental and theoretical investigations have been performed (see Reference 2 for a recent overview). Panel and Euler methods have frequently been used, while recently Navier–Stokes methods have been employed.

Explicit predictor–corrector,[3] implicit approximate factorization[4] and upwind relaxation[5] time-stepping schemes using finite difference and finite volume space discretizations have already been applied to solve the three-dimensional compressible Navier–Stokes equations for flow over delta wings.[6–8] The comparison with experimental data demonstrated the realism of the simulations for subsonic and supersonic steady flow. Maximum lift and vortex breakdown were predicted, in close agreement with wind tunnel measurements for subsonic flow.[8, 9]

* Current address: DFVLR, Bunsenstr. 10, D-3400 Göttingen, F.R.G.

0271–2091/89/080943–20$10.00

Received 13 June 1988

Explicit Runge–Kutta time-stepping methods using the finite volume space discretization were first developed for the numerical solution of the Euler equations.[10, 11] Later the methods were extended to solve the Navier–Stokes equations,[12–18] discretizing the velocity and temperature gradients as well as div **u** on cell interfaces either by local co-ordinate transformations or by averaging over straddling cells, in either case involving 19 cells in three dimensions.

In the present paper, laminar transonic flow over the 65° round leading edge delta wing proposed for the International Vortex Flow Experiment on Euler Code Validation (the subject of the International Vortex Flow Symposium held in Stockholm on 1–3 October 1986) is simulated at $M_\infty = 0{\cdot}85$, $\alpha = 10°$, $Re_{\infty, c_R} = 2{\cdot}38 \times 10^6$ and $Re_{\infty, \mathrm{SPAN}} = 10^m$ ($m = 5$, 6, 7). The compressible Navier–Stokes equations (Section 2) are discretized using the finite volume technique in space involving 25 cells to form the viscous flux difference as opposed to the conventional 19 cells. Non-linear second-order and linear fourth-order damping terms are added to the physical difference operator. The resulting system of ordinary differential equations is solved by an explicit three-stage Runge–Kutta scheme in time. A linear stability condition is derived for a scalar model equation to determine the local time steps and the allowable damping coefficients (Section 3). The 65° swept delta wing has 15% taper and is defined by one section with 0·7% nose radius and with 5% thickness at 40% local chord. The fine O–O-type mesh has 129, 49 and 65 grid points in the chordwise, near-normal and spanwise directions respectively (Section 4). The delta wing surface is assumed to be adiabatic. Locally one-dimensional characteristic boundary conditions are used in the far-field (Section 5). Results are presented for the above mentioned cases and compared with experiment and the Euler solution (Section 6).

2. GOVERNING EQUATIONS

Fluid motion is governed by the conservation laws for mass, momentum and energy. The fluid investigated here is a perfect gas obeying Newton's and Fourier's laws. External forces and heat sources are not taken into account. For an arbitrary stationary cell V with boundary ∂V and outer normal unit vector $\mathbf{n}$ in an absolute frame of reference, the Navier–Stokes equations read[19]

$$\int_V \frac{\partial \mathbf{Q}}{\partial t} \, \mathrm{d}V + \int_{\partial V} \mathbf{H} \cdot \mathbf{n} \, \mathrm{d}A = 0, \tag{1}$$

where

$$\mathbf{Q} = \begin{pmatrix} \rho \\ \rho \mathbf{u} \\ e \end{pmatrix} \qquad \mathbf{H} = \begin{pmatrix} \rho \mathbf{u} \\ \rho \mathbf{u}\,\mathbf{u} + p\mathbf{I} - \boldsymbol{\tau} \\ (e+p)\mathbf{u} - \boldsymbol{\tau} \cdot \mathbf{u} + \mathbf{q} \end{pmatrix}.$$

$\mathbf{Q}$ is the vector of the conservative variables, i.e. density, momentum density and total energy density. $\mathbf{H}$ represents the flux tensor, $\mathbf{I}$ the unit tensor. Pressure p and temperature T are related to the conservative variables by the equations of state for a perfect gas with the ratio of constant specific heats $\gamma = 1{\cdot}4$. The stress tensor is given by Newton's law:

$$\boldsymbol{\tau} = \mu[\mathrm{grad}\, \mathbf{u} + (\mathrm{grad}\, \mathbf{u})^{\mathrm{T}}] + \lambda \,\mathrm{div}\, \mathbf{u}\, \mathbf{I}. \tag{2}$$

Fourier's law states for the heat flux

$$\mathbf{q} = -\kappa \,\mathrm{grad}\, T. \tag{3}$$

The viscosity coefficients μ and λ are related by Stokes' hypothesis. The Prandtl number is assumed to be constant, namely $Pr = 0{\cdot}72$, thus giving a simple relationship between the thermal conductivity coefficient κ and the viscosity coefficient μ. The dependence of μ on the temperature T is obtained from the Sutherland law with the Sutherland constant $S/T_\infty = 0{\cdot}375$.

A spatial vector is expressed in Cartesian co-ordinates x, y and z, i.e. chordwise from the apex, spanwise from the plane of bilateral symmetry and normal from the wing plane respectively. A velocity vector $\mathbf{u}$ is represented by its components u, v and w in the corresponding co-ordinate directions.

3. NUMERICAL METHOD

Spatial discretization

The Navier–Stokes equations (1) are discretized in hexahedrons (Figure 1) using the finite volume technique.[3] Since the conservative variables are assumed to be defined by their cell averages, the volume integral in (1) over a cell P is expressed by

$$\int_{V_P} \frac{\partial \mathbf{Q}}{\partial t}\, \mathrm{d}V = \frac{\partial \mathbf{Q}_P}{\partial t} \int_{V_P} \mathrm{d}V. \tag{4}$$

The surface integral in (1) over the boundary of cell P is approximated by assuming the mean value of the flux tensor on each side to be equal to the arithmetic average of the flux tensor in the adjacent cells:

$$\int_{\partial V_P} \mathbf{H}\cdot\mathbf{n}\,\mathrm{d}A \simeq \sum_{k=1}^{6} \mathbf{H}_{Pk}\cdot \int_{\partial V_{Pk}} \mathbf{n}\,\mathrm{d}A, \tag{5}$$

where

$$\mathbf{H}_{Pk} = \tfrac{1}{2}(\mathbf{H}_P + \mathbf{H}_k).$$

∂V_{Pk} denotes the common part of the boundaries of P and its neighbouring cell k. The cell volume in (4) is computed as the sum of five tetrahedra.[20] The surface normal in (5) is determined as the sum of the surface normals of two triangles.[21]

With the conservative variables given, all terms of the flux tensor are readily available in cell P, except for the gradients of the velocity components and temperature as well as div $\mathbf{u}$. Following the

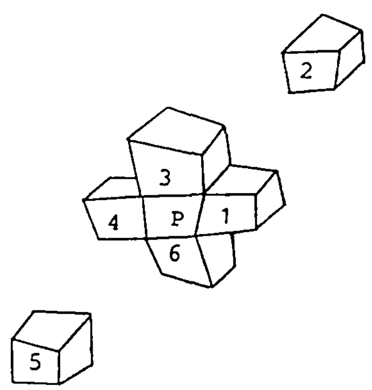

Figure 1. Basic hexahedron P and neighbouring cells 1 to 6 (2 and 5 set apart)

definition of the conservative variables as cell averages, the gradients in cell P are defined by

$$\operatorname{grad}\phi_P = \int_{V_P} \operatorname{grad}\phi \,\mathrm{d}V \bigg/ \int_{V_P} \mathrm{d}V, \tag{6}$$

where $\phi = u$, v, w or T.

Using the gradient theorem, the volume integral in (6) can be expressed by a surface integral, which is approximated similarly to (5):[22]

$$\operatorname{grad}\phi_P = \int_{V_P} \phi\,\mathbf{n}\,\mathrm{d}A \bigg/ \int_{V_P} \mathrm{d}V \simeq \sum_{k=1}^{6} \phi_{Pk} \int_{\partial V_{Pk}} \mathbf{n}\,\mathrm{d}A \bigg/ \int_{V_P} \mathrm{d}V, \tag{7}$$

where

$$\phi_{Pk} = \tfrac{1}{2}(\phi_P + \phi_k).$$

div $\mathbf{u}_P$ is evaluated similarly to grad ϕ_P.

On a Cartesian equidistant grid, the present finite volume approximation is equivalent to a second-order central difference discretization involving 25 points as opposed to the conventional 19 points. The approximation of the viscous terms is consistent with the flux tensor averaging (5). The use of local co-ordinate transformations and the definition of straddling cells are avoided. Instead, the Cartesian derivatives of velocity and temperature are cell-averaged and therefore rot $\mathbf{u}$ is also directly given for each cell, a useful property, e.g. for the application of the Baldwin–Lomax turbulence model. Norton *et al.*[23] have also considered this same approximation.

Numerical damping

The spatial discretization constitutes the physical difference operator $\mathbf{F}_{\mathrm{PH}}$ defined by the right-hand side of (5) divided by the cell volume. These central differences do not damp unphysical oscillations caused by flow discontinuities and waves with short wavelengths. The numerical damping terms, which are therefore added to $\mathbf{F}_{\mathrm{PH}}(\mathbf{Q})$, comprise non-linear second-order differences sensed by the discretized second derivative of the pressure, and linear fourth-order differences of the conservative variables:[20]

$$\mathbf{F}_{\mathrm{N}}(\mathbf{Q}) = (\mathrm{CFL}/\Delta t)\{\chi(\delta_I[s_I(p)\delta_I] + \delta_J[s_J(p)\delta_J] + \delta_K[s_K(p)\delta_K]) - \Lambda(\delta_I^4 + \delta_J^4 + \delta_K^4)\}\mathbf{Q}, \tag{8}$$

with CFL the maximum CFL number used (see the subsection on stability below) and Δt the time step. The constants χ and Λ lie in the ranges $0 \leqslant \chi \leqslant 0{\cdot}005$ and $0{\cdot}005 \leqslant \Lambda \leqslant 0{\cdot}02$ (see the subsection on stability below). The sensors s_I, s_J and s_K are of similar form, e.g. s_I for a cell indexed by I, J, K is given by

$$s_I(p_{I\pm 1/2,J,K}) = \mu_I|\delta_I^2 p_{I\pm 1/2,J,K}| \bigg/ \max_{I',J',K'} \left|\delta_I^2 p_{I',J',K'}\right|. \tag{9}$$

The classical finite difference operators are defined by

$$\begin{aligned} \delta_I a_{I,J,K} &= a_{I+1/2,J,K} - a_{I-1/2,J,K}, \\ \mu_I a_{I,J,K} &= (a_{I+1/2,J,K} + a_{I-1/2,J,K})/2 \end{aligned} \tag{10}$$

and similarly for J and K.

The numerical damping operator $\mathbf{F}_{\mathrm{N}}$ is modified near the wing surface and in the far-field to ensure its dissipative property there also.[24] Using the periodic and symmetry boundary conditions (see Section 5), $\mathbf{F}_{\mathrm{N}}$ can be determined near these boundaries without modifying (8) or (9).

Time integration

Thus the semidiscrete approximation of the Navier–Stokes equations can be written as

$$\mathrm{d}\mathbf{Q}/\mathrm{d}t=\mathbf{F}(\mathbf{Q}), \tag{11}$$

where

$$\mathbf{F}=\mathbf{F}_{\mathrm{PH}}+\mathbf{F}_{\mathrm{N}}.$$

Equation (11) represents a large system of first-order ordinary differential equations. It is solved for the steady state by the second-order explicit three-stage Runge–Kutta scheme:[25]

$$\begin{aligned}
&\mathbf{Q}^{(0)}=\mathbf{Q}^{n},\\
&\mathbf{Q}^{(1)}=\mathbf{Q}^{(0)}+\Delta t\,\mathbf{F}(\mathbf{Q}^{(0)}),\\
&\mathbf{Q}^{(2)}=\mathbf{Q}^{(0)}+\Delta t[(1-\theta)\,\mathbf{F}(\mathbf{Q}^{(0)}+\theta\,\mathbf{F}(\mathbf{Q}^{(1)})],\\
&\mathbf{Q}^{(3)}=\mathbf{Q}^{(0)}+\Delta t[(1-\theta)\,\mathbf{F}(\mathbf{Q}^{(0)})+\theta\,\mathbf{F}(\mathbf{Q}^{(2)})],\\
&\mathbf{Q}^{n+1}=\mathbf{Q}^{(3)},
\end{aligned} \tag{12}$$

with $\theta=1/2$; n denotes the time level.

Stability

The stability of explicit Runge–Kutta schemes applied to the semidiscretization (11) of the Navier–Stokes equations (1) is studied for the scalar model equation

$$\begin{aligned}
\frac{\partial a}{\partial t}+\lambda_\xi\frac{\partial a}{\partial \xi}+\lambda_\eta\frac{\partial a}{\partial \eta}+\lambda_\zeta\frac{\partial a}{\partial \zeta}=\nu_\xi\frac{\partial^2 a}{\partial \xi^2}+\nu_\eta\frac{\partial^2 a}{\partial \eta^2}+\nu_\zeta\frac{\partial^2 a}{\partial \zeta^2}+\nu_{\xi\eta}\frac{\partial^2 a}{\partial \xi\partial\eta}+\nu_{\xi\zeta}\frac{\partial^2 a}{\partial \xi\partial\zeta}\\
+\nu_{\eta\zeta}\frac{\partial^2 a}{\partial \eta\partial\zeta}+\varepsilon_\xi\frac{\partial^4 a}{\partial \xi^4}+\varepsilon_\eta\frac{\partial^4 a}{\partial \eta^4}+\varepsilon_\zeta\frac{\partial^4 a}{\partial \zeta^4},
\end{aligned} \tag{13}$$

where

$$\begin{aligned}
&\lambda_h=|\mathbf{u}\cdot\mathrm{grad}\,h|+c|\mathrm{grad}\,h|,\\
&\nu_h=\nu\,\mathrm{grad}\,h\cdot\mathrm{grad}\,h+\Delta h^2\chi_h\,\mathrm{CFL}/\Delta t,\\
&\nu_{hg}=2\nu|\mathrm{grad}\,h\cdot\mathrm{grad}\,g|+\frac{\lambda+\mu}{\rho}|\mathrm{grad}\,h|\,|\mathrm{grad}\,g|,\\
&\varepsilon_h=-\Delta h^4\,\Lambda\,\mathrm{CFL}/\Delta t,
\end{aligned}$$

with c the speed of sound and

$$\nu=\max\{\mu,\lambda+2\mu,\mu\gamma/Pr\}/\rho,\qquad \chi_h=\chi s_h,\qquad h,g\in\{\xi,\eta,\zeta\}.$$

Equation (13) is derived from the differential form of the Navier–Stokes equations in transformed co-ordinates ξ, η and ζ[19] by linearization and from the differential expressions of the damping terms in (8). λ_h is chosen equal to the maximum modulus of the eigenvalues belonging to the Jacobian matrix of the flux in the h-direction. ν_h and ν_{hg} are determined by the maximum moduli of the eigenvalues belonging to the coefficient matrices of the second derivatives $\partial^2/\partial h^2$ and $\partial^2/\partial h\partial g$ respectively in the linearized Navier–Stokes equations, including the differential expressions of the linearized second-order damping terms. ε_h represents the coefficient of the fourth-order damping term in the h-direction. Thus the scalar ansatz (13) models the full Navier–Stokes equations including the numerical damping terms, whereas inviscid, diffusion and mixed-derivative vector parts of the linearized Navier–Stokes equations are considered separately in References 26–28 to determine the respective time steps of time-splitting schemes.

The first and second spatial derivatives in (13) are discretized by second-order central finite differences corresponding to the finite volume approximation (11):

$$\left.\frac{\partial a}{\partial h}\right|_{I,J,K}=\frac{1}{\Delta h}\,\mu_h\,\delta_h\,a_{I,J,K}+O(\Delta h^2), \tag{14a}$$

$$\left.\frac{\partial a^2}{\partial h^2}\right|_{I,J,K}=\frac{1}{\Delta h^2}\,(\mu_h\delta_h)^2\,a_{I,J,K}+O(\Delta h^2), \tag{14b}$$

$$\left.\frac{\partial^2 a}{\partial h\partial g}\right|_{I,J,K}=\frac{1}{\Delta h\Delta g}\,\mu_h\delta_h\mu_g\delta_g a_{I,J,K}+O(\Delta h^2). \tag{14c}$$

The finite difference operators in (14) are defined by (10) with ξ corresponding to I, η to J and ζ to K. The fourth derivatives in (13) are discretized according to (8).

Note that $a_{I\pm 1,J,K}$, $a_{I,J\pm 1,K}$ and $a_{I,J,K\pm 1}$ do not appear in (14b). The second-order truncation error in (14b) is four times greater than that which would be obtained if the compact differencing δ_h^2 were used instead of $(\mu_h\delta_h)^2$.

The linear stability of an explicit Runge–Kutta scheme is investigated for application to the model equation (13) with frozen coefficients and spatially discretized by (14). The analysis shows that the shortest resolvable waves are undamped by (14b), in contrast to the compact differencing δ_h^2. The stability condition reads

$$|\mathrm{RK}|\left\{\left[\frac{\tilde{\nu}_\xi}{\Delta\xi^2}+\frac{\tilde{\nu}_\eta}{\Delta\eta^2}+\frac{\tilde{\nu}_\zeta}{\Delta\zeta^2}+\frac{\nu_{\xi\eta}}{\Delta\xi\Delta\eta}+\frac{\nu_{\xi\zeta}}{\Delta\xi\Delta\zeta}+\frac{\nu_{\eta\zeta}}{\Delta\eta\Delta\zeta}-16\left(\frac{\varepsilon_\xi}{\Delta\xi^4}+\frac{\varepsilon_\eta}{\Delta\eta^4}+\frac{\varepsilon_\zeta}{\Delta\zeta^4}\right)\right]^{-1}\right\}, \tag{15}$$

where

$$\tilde{\nu}_h=\alpha\nu\,\mathrm{grad}\,h\cdot\mathrm{grad}\,h+4\Delta h^2\chi_h\,\mathrm{CFL}/\Delta t,$$

with $\alpha=1$ for (14b) but $\alpha=4$ for the compact differencing δ_h^2.

The negative and positive stability bounds RK and CFL are chosen such that all complex numbers z with $\mathrm{RK}\leqslant Re(z)\leqslant 0$ and $|\mathrm{Im}(z)|\leqslant\mathrm{CFL}$ lie inside the stability region of the Runge–Kutta method. For the three-stage Runge–Kutta method (12) the following choice is made: $\mathrm{CFL}=1{\cdot}5$, $\mathrm{RK}=-1$ (Figure 2).

The viscous contributions in (15) (denoted here by S) involving the coefficient ν and the second- and fourth-order damping coefficients in (15) (here referred to as D_2 and D_4) share the negative real axis of the stability region. Their distribution may be prescribed by

$$S\Delta t\leqslant\beta_1|\mathrm{RK}|, \tag{16a}$$

$$D_2\Delta t\leqslant\beta_2|\mathrm{RK}|, \tag{16b}$$

$$D_4\Delta t\leqslant\beta_3|\mathrm{RK}|, \tag{16c}$$

where $0\leqslant\beta_i$ and $\sum_{i=1}^{3}\beta_i=1$. Equations (16b) and (16c) yield the following conditions for the damping coefficients:

$$\chi\leqslant(\beta_2/4d)|\mathrm{RK}|/\mathrm{CFL}, \tag{17a}$$

$$\Lambda\leqslant(\beta_3/16d)|\mathrm{RK}|\mathrm{CFL}, \tag{17b}$$

with d the dimension, i.e. $d=3$ for 3D.

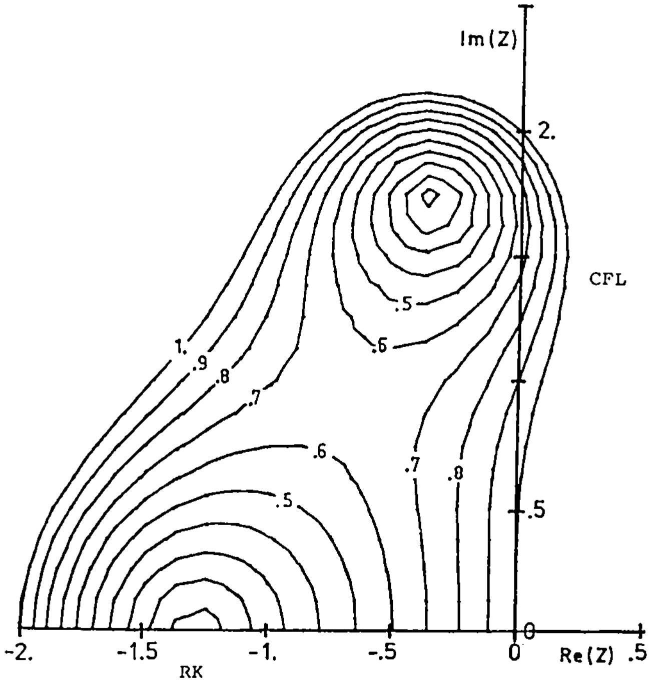

Figure 2. Contours of constant modulus of growth factors of (12) and stability bounds RK and CFL

Then, using (16a) in (15), the stability condition is obtained:

$$\Delta t \leqslant \min\left\{\mathrm{CFL}\left[\frac{|\lambda\xi|}{\Delta\xi}+\frac{|\lambda\eta|}{\Delta\eta}+\frac{|\lambda\zeta|}{\Delta\zeta}\right]^{-1},\right.$$

$$\left.\beta_1|\mathrm{RK}|\left[\frac{v_{\xi\xi}}{\Delta\xi^2}+\frac{v_{\eta\eta}}{\Delta\eta^2}+\frac{v_{\zeta\zeta}}{\Delta\zeta^2}+\frac{v_{\xi\eta}}{\Delta\xi\Delta\eta}+\frac{v_{\xi\zeta}}{\Delta\xi\Delta\zeta}+\frac{v_{\eta\zeta}}{\Delta\eta\Delta\zeta}\right]^{-1}\right\}, \tag{18}$$

where

$$v_{hh}=\alpha v \operatorname{grad} h\cdot\operatorname{grad} h,$$

with $\alpha=1$ for (14b) but $\alpha=4$ for the compact differencing δ_h^2.

In order to apply the stability condition (18) to the finite volume discretization, the metric terms are related to geometrical quantities:[29]

cell volume

$$\Delta\xi\Delta\eta\Delta\zeta J^{-1}=v=\int_V \mathrm{d}V, \tag{19a}$$

surface normal in G-direction

$$\Delta\xi\Delta\eta\Delta\zeta J^{-1}\operatorname{grad} g/\Delta g=\mathbf{S}_G=\int_{\partial V_G}\mathbf{n}\,\mathrm{d}A, \tag{19b}$$

where $g=\xi,\eta,\zeta$ corresponds to $G=I, J, K$ and ∂V_G denotes a cell boundary with constant G. J represents the Jacobian determinant of the transformation $(\xi,\eta,\zeta)^{\mathrm{T}}$ (x,y,z).

Thus the stability condition (18) with (17a) and (17b) for an explicit Runge–Kutta method like (12) applied to the finite volume discretization of the Navier–Stokes equations (11) reads

$$\begin{aligned}\Delta t \leqslant \min\{&\mathrm{CFL}\ \nu\,[|\mathbf{u}\cdot\mathbf{S}_I| + c|\mathbf{S}_I| + |\mathbf{u}\cdot\mathbf{S}_J| + c|\mathbf{S}_J| + |\mathbf{u}\cdot\mathbf{S}_K| + c|\mathbf{S}_K|]^{-1},\\ &\beta_1\,|\mathrm{RK}|\nu^2[\nu\{\alpha(\mathbf{S}_I\cdot\mathbf{S}_I + \mathbf{S}_J\cdot\mathbf{S}_J + \mathbf{S}_K\cdot\mathbf{S}_K) + 2(|\mathbf{S}_I\cdot\mathbf{S}_J| + |\mathbf{S}_I\cdot\mathbf{S}_K| + |\mathbf{S}_J\cdot\mathbf{S}_K|)\}\\ &+ [(\lambda+\mu)/\rho]\,(|\mathbf{S}_I|\,|\mathbf{S}_J| + |\mathbf{S}_I|\,|\mathbf{S}_K| + |\mathbf{S}_J|\,|\mathbf{S}_K|)]^{-1}\},\end{aligned} \tag{20}$$

with $\alpha = 1$.

If the compact differencing δ_h^2 were used instead of (14b), the stability condition would be more restrictive, since $\mathbf{S}_I\cdot\mathbf{S}_I + \mathbf{S}_J\cdot\mathbf{S}_J + \mathbf{S}_K\cdot\mathbf{S}_K$ would have to be multiplied by $\alpha = 4$.

$\beta_1 = 1/2$, $\beta_2 = 1/30$ and $\beta_3 = 1/2$ were used in (17) and (20) for the present calculation with CFL = 0·5 and RK = −1. Although $\sum_{l=1}^{3}\beta_l > 1$, stability was maintained, indicating that the stability bound RK could have been chosen lower than −1 for the Runge–Kutta method (12). For the $65\times25\times33$ medium mesh, CFL = 1·5, RK = −1, $\beta_1 = 1/2$, $\beta_2 = 1/10$ and $\beta_3 = 3/2$ were used. Computational work is saved by computing the local time steps according to (20) only at those time levels which are powers of two.

4. MESH

The round leading edge delta wing proposed for the International Vortex Flow Experiment on Euler Code Validation has 65° sweep and 15% taper. It is defined by one section in terms of x- and z-co-ordinates, i.e. chordwise from the leading ledge and normal from the wing plane respectively, non-dimensionalized by the local chord:

$$z = \begin{cases} \pm[0{\cdot}1183\sqrt{x} - 0{\cdot}2101\,x + 0{\cdot}3501\,x^2 - 0{\cdot}3406x & \text{for}\quad 0 \leqslant x \leqslant 0{\cdot}4,\\ \text{NACA 64A005} \quad \text{for} \quad 0{\cdot}4 \leqslant x \leqslant 1. \end{cases} \tag{21}$$

The nose radius is 0·7%, the maximum thickness at 40% is 5% local chord and the trailing edge is sharp.

The O–O mesh topology introduces periodic, symmetry, wing and far-field boundaries to determine bilaterally symmetric flow over a quadrilateral wing. The symmetry boundary lies in the $y = 0$ plane. A hemisphere with a radius of three root chord lengths from root mid-chord is chosen as the far-field boundary. The periodic boundaries extend from the trailing edge and tip of the wing in the positive x- and y-directions respectively.

The O–O meshes are generated by the transfinite interpolation method.[30] The fine mesh consists of 129, 49 and 65 grid points in the chordwise (I-direction), near-normal (J-direction) and spanwise (K-direction) respectively, i.e. 410 865 grid points in total. On the wing the mesh points are clustered near the leading edge and tip, and to a lesser extent also near the trailing edge and symmetry boundary, with larger spacings in the mid-sections (Figure 3). On the hemisphere in the far-field the grid points are distributed equally (Figures 4 and 5), except for a clustering near the two points lying on the two parabolic singular lines extending from the tip leading and trailing edges.[30] The mesh is nearly orthogonal at the wing contour, except for the points near the trailing edge and tip. The grid points between wing contours and far-field are clustered near the wing to resolve the boundary layer for the respective Reynolds number (Figures 4 and 5 for $Re_{\infty,\mathrm{CR}} = 2{\cdot}38\times10^6$). For $Re_{\infty,\mathrm{SPAN}} = 10^m$ ($m = 5, 6, 7$) $65\times25\times33$ medium grids have been used, each with a different clustering in the near-normal direction.

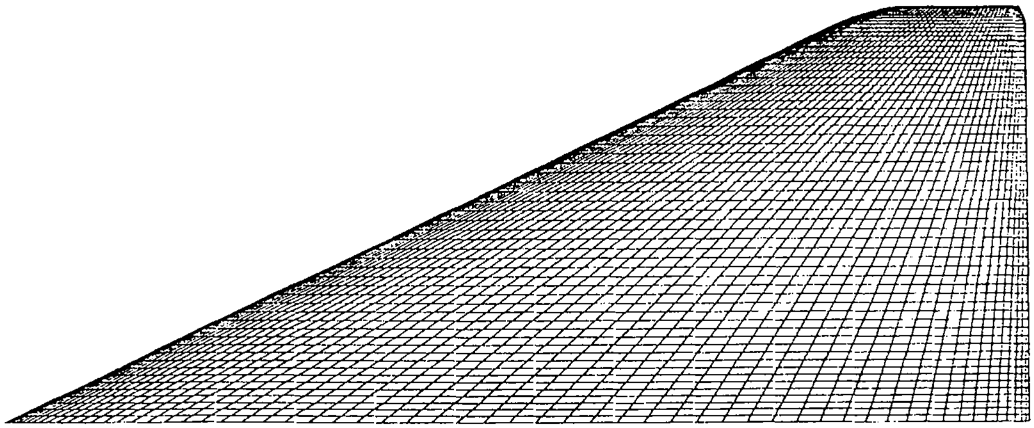

Figure 3. Surface mesh of 65° swept cropped delta wing

5. INITIAL AND BOUNDARY CONDITIONS

For $M_\infty = 0{\cdot}85$, $\alpha = 10^0$ and $Re_{\infty,\mathrm{SPAN}} = 10^5$ the calculation is started from freestream on the course mesh obtained by cancelling every other point of the medium (53 625 grid points) mesh. Then the result is interpolated on the medium mesh and 500 time steps are taken to obtain the result on the medium mesh. This result is used as the initial condition for the next higher Reynolds number, etc.

For $M_\infty = 0{\cdot}85$, $\alpha = 10^0$ and $Re_{\infty,\mathrm{CR}} = 2{\cdot}38 \times 10^6$ the calculation is started from freestream on a coarse mesh using a large second-order damping coefficient ($\chi = 0{\cdot}1$) which is subsequently reduced. The converged result is interpolated on the medium mesh and so on to the fine mesh.

At periodic boundaries grid points on upper and lower surfaces are mapped onto each other. For the conservative variables to be uniquely defined, the periodic boundary condition requires

$$\mathbf{Q}_{IMAX,J,K} = \mathbf{Q}_{1,J,K}, \qquad \mathbf{Q}_{I,J,KMAX} = \mathbf{Q}_{IMAX-I,J,KMAX-1}. \tag{22}$$

At the symmetric boundary ρ, u, w and e are even functions with respect to y, and v is odd:

$$(\rho, u, v, w, e)^{\mathrm{T}}(x, y, z) = (\rho, u, -v, w, e)^{\mathrm{T}}(x, -y, z). \tag{23}$$

The no-slip condition holds on the wing, which is assumed to be adiabatic. The pressure is obtained by neglecting the viscous terms in the wall normal momentum equation:

$$\mathbf{u}_{\mathrm{w}} = \mathbf{0}, \qquad \left.\frac{\partial T}{\partial n}\right|_{\mathrm{w}} = 0, \qquad \left.\frac{\partial p}{\partial n}\right|_{\mathrm{w}} = 0. \tag{24}$$

The pressure and the stress tensor at the wing interface of the first cell above the wing are approximated by their values in that cell.

The boundary conditions at the far-field boundary are based on the theory of characteristics for locally one-dimensional inviscid flow.[31] For supersonic inflow or outflow the locally one-dimensional Riemann invariants, entropy and tangential velocity component, i.e. (with the speed of sound c)

$$R_1 = \mathbf{u}\cdot\mathbf{n} - \frac{2}{\gamma - 1}c, \qquad R_2 = \mathbf{u}\cdot\mathbf{n} + \frac{2}{\gamma-1}c,$$

$$R_3 = \ln(p/\rho^\gamma), \qquad \mathbf{R}_4 = \mathbf{u} - (\mathbf{u}\cdot\mathbf{n})\mathbf{n}, \tag{25a}$$

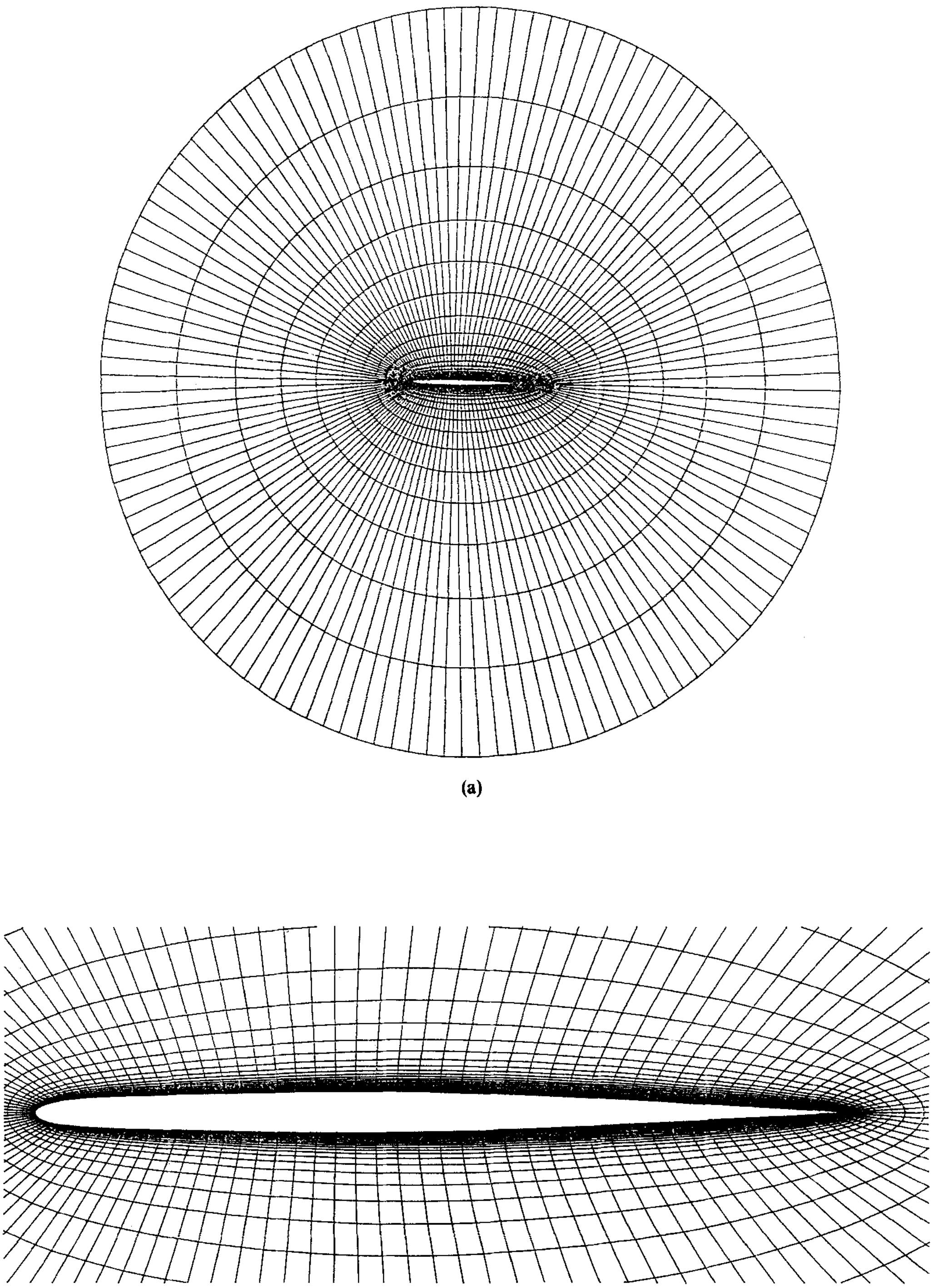

(a)

(b)

Figure 4. Mesh in plane of symmetry

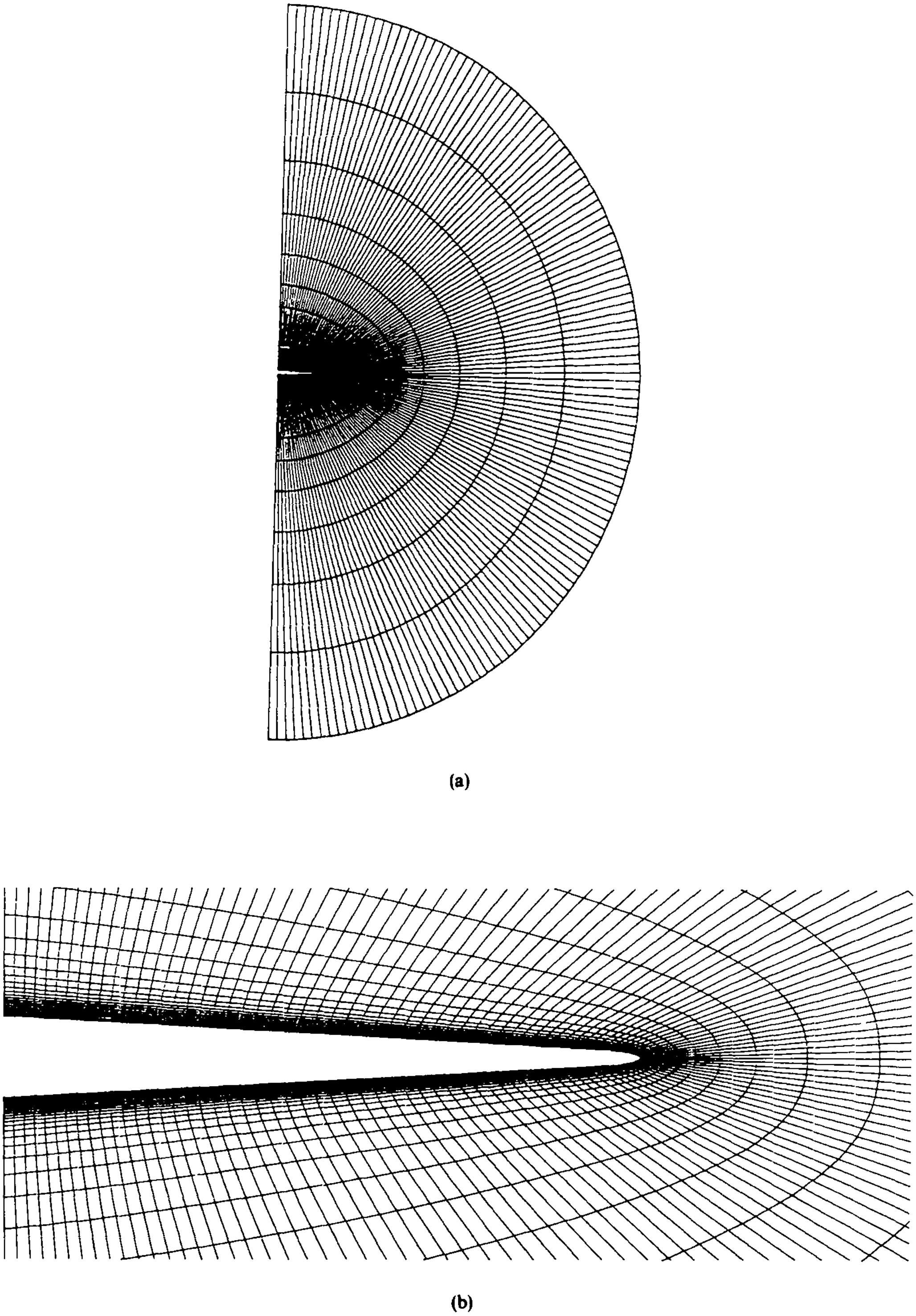

Figure 5. Mesh in surfaces $I = 33$ and 97 seen from behind (at $\sim 37\%$ local chord on wing)

are given from outside or inside the region of interest respectively by

$$R_m = R_{m_\infty}, \qquad \partial R_m/\partial n = 0. \tag{25b}$$

For subsonic inflow R_1, R_3 and $\mathbf{R}_4$ are given from outside and R_2 from inside. For subsonic outflow R_2, R_3 and $\mathbf{R}_4$ are determined from inside and R_1 from outside.

The conditions (25b) are used to determine R_m in a fictitious cell outside the domain of integration either by freestream or by R_m in the cell next to the far-field.

6. RESULTS

A computer program has been developed based on the Runge–Kutta finite volume method for the three-dimensional Navier–Stokes equations. The code is implemented on the CYBER 205 (two pipes and eight million words of memory) of the Scientific Information Service in Kansas City, MO. The fine-mesh computations were performed on the CYBER 205 of the Minnesota Supercomputer Center located at the University of Minnesota. The vector-coding concept of Reference 32 is employed to fully vectorize the computer program. Using half-precision and a fine $129 \times 49 \times 65$ mesh, the latest version takes 23×10^{-6} CPU seconds per time step and per grid point.

Laminar flow over the 65° swept round leading edge cropped delta wing described in Section 4 has been simulated at $M_\infty = 0{\cdot}85$, $\alpha = 10^0$ and $Re_{\infty, c_R} = 2{\cdot}38 \times 10^6$ (based on root chord c_R).

The convergence history (Figure 6, top) shows a rapid decrease of the density change in the coarse and medium mesh. The 'spikes' are due to the normalization $\|\rho^n - \rho^{n-1}\|_2 / \|\rho^1 - \rho^0\|_2$ at restarts and to interpolations from coarser to finer grids. The convergence in the fine mesh is poor because the CFL number had to be decreased from 1·5 and 1 to 0·5 to allow a larger second-order damping coefficient χ (see (17a)) in the first cycles on the fine mesh. Decreasing χ had a negative effect on convergence but apparently no effect on lift and drag, except for the coarse mesh (Figure 6, bottom). On each mesh level C_L and C_D become constant and the density change is deemed low enough to assume steady flow results.

Comparison of the lift, drag and pitching moment (around $x/c_R = 0{\cdot}57$) coefficients for the different mesh levels (Table I) shows that the coarse ($33 \times 13 \times 17$) mesh underpredicts C_L and C_D considerably. The medium-mesh C_L and the fine-grid C_D happen to be closest to the experiment[33] measured at the higher Reynolds number $Re_{\infty, c_R} = 9 \times 10^6$.

The pressure coefficients at the stations $x/c_R = 0{\cdot}3$, 0·6, 0·9 and 0·95 and $2y/b = 0{\cdot}55$ (b denotes span; see Figure 7) are compared with experimental data[34] at $Re_{\infty, c_R} = 2{\cdot}38 \times 10^6$ and Euler solutions[35] with 10^6 points. $s(x)$ denotes the local semi-span, $l(y)$ the local chord and x_{LE} the local leading edge x-component. The location of the primary vortex core is predicted in good agreement with the experiment, whereas the pressure minimum in the Euler solution lies too close to the leading edge (Figure 8). The pressure level under the primary vortex core is predicted correctly with the fine mesh, while the medium mesh overpredicts the pressure, probably because of poor vortex resolution (e.g. at $2y/b = 0{\cdot}55$ in Figure 8).[36]

Between the primary and secondary separation cores at $x/c_R = 0{\cdot}3$, 0·6 and 0·8 the pressure is overpredicted with the fine grid as well, and the pressure under the secondary vortex core is lower than in the experiment. At x/c_R a pressure rise can be seen close to the leading edge. That pressure increase is neither apparent in the medium-mesh solution[36] nor in the experiment. Even with finer meshes, however, complete agreement cannot be expected from a laminar computation, because the flow was observed to be transitional in the experiment. Moreover, the wind tunnel model was a wing–body combination on the windward side.

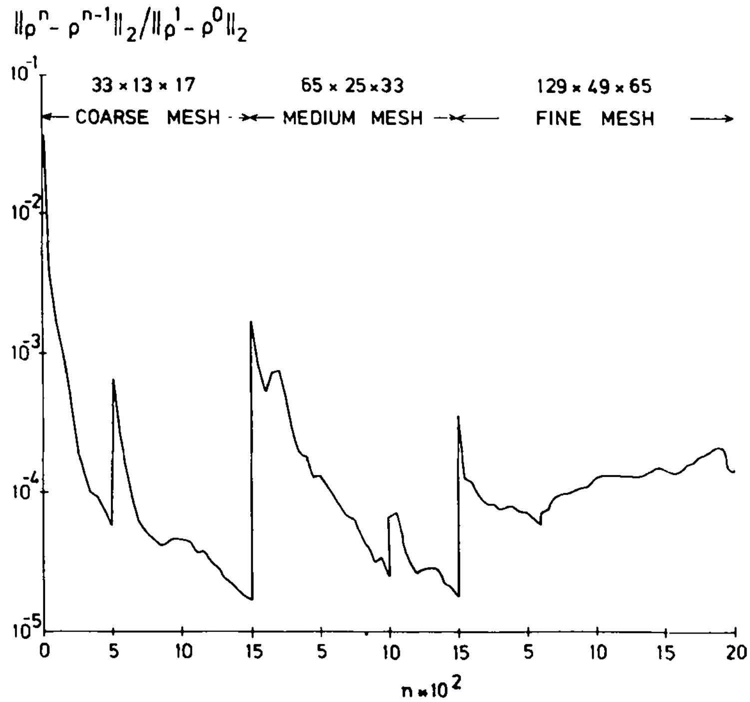

(a)

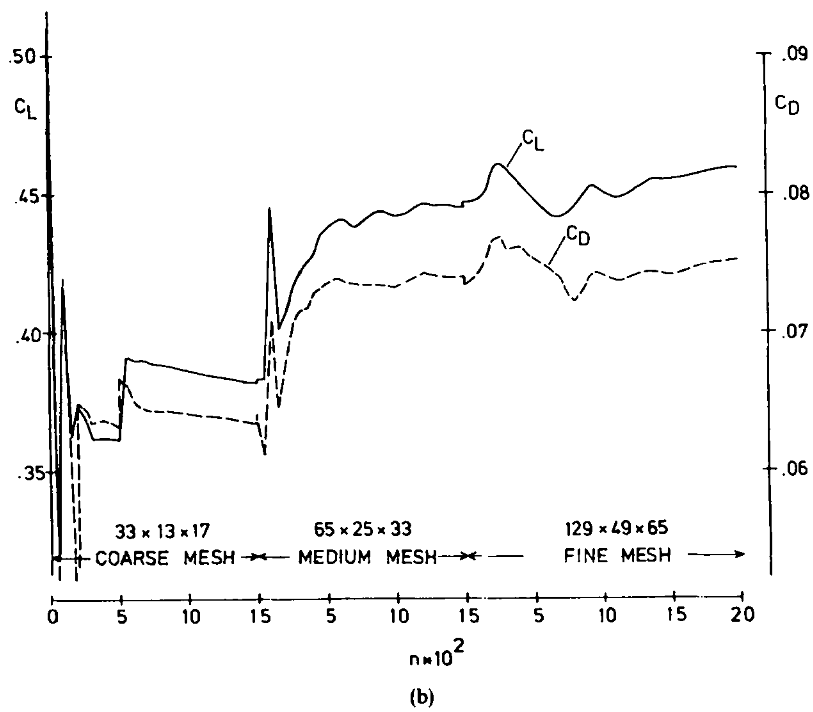

(b)

Figure 6. Convergence history for $M_\infty = 0{\cdot}85$, $\alpha = 10^0$ and $Re_{\infty,c_R} = 2{\cdot}38 \times 10^6$

Table I. Comparison of integral values for $M_\infty = 0{\cdot}85$, $\alpha = 10^0$, $Re_{\infty, c_R} = 2{\cdot}38 \times 10^6$ (9×10^6 in experiment)

Mesh	C_L	C_D	C_m
Coarse $33 \times 13 \times 17$	0·3811	0·0633	−0·0088
Medium $65 \times 25 \times 33$	0·4466	0·0741	−0·0108
Fine $129 \times 49 \times 65$	0·4586	0·0752	−0·0098
Experiment[33]	0·4386	0·0755	−0·0073

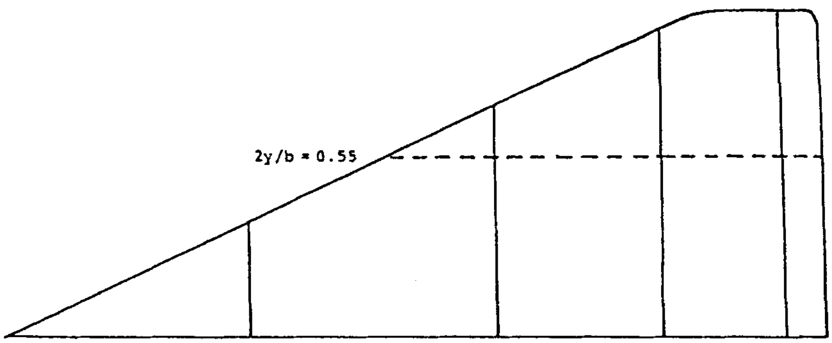

Figure 7. Stations $x/c_R = 0{\cdot}3$, 0·6, 0·8, 0·95 and $2y/b = 0{\cdot}55$

Figure 9 shows pressure coefficient, Mach number and total pressure $(1 - p_0/p_{0_\infty})$ contours as well as velocity vectors at $x/c_R = 0{\cdot}3$, 0·6, 0·8 and 0·95. The growth of the primary vortex can be well identified. However, the secondary vortex is hardly visible, even in the enlargement of the velocity vectors near the leading edge and tip. Note that the velocity vectors in Figures 9 and 10 are not given at mesh points but are interpolated to a Cartesian mesh. The structure of the primary vortex can be seen in a chordwise cut in Figure 10.

In Figure 11(a) the secondary separation line at $y/s(x) \sim 0{\cdot}74$ is indicated by the line towards which the skin friction lines converge. The skin friction lines emanating from points a short distance away from the tip and trailing edge turn in an upstream direction and apparently terminate in a nodal point of separation on the secondary separation line.

The pressure minimum (Figure 11(b)) almost coincides with the secondary separation line, around which large gradients of the modulus of vorticity (Figure 11(c)) can be seen. Pressure and vorticity are nearly conical up to $x/c_R \sim 0{\cdot}55$. Their gradients near the leading edge between $x/c_R \sim 0{\cdot}55$ and $\sim 0{\cdot}75$ might be indicative of a tertiary separation vortex (cf. $x/c_R = 0{\cdot}6$ in Figure 8).

The streamlines (Figure 12) show two distinct vortices which lift before the trailing edge.

The velocity vectors in grid surfaces (at $\sim 37\%$ local chord on the wing) seen from behind show the flow directions (Figure 13). On the leeward side the boundary layer flow is directed in a clockwise direction from the symmetry plane up to the secondary separation line, where it meets the flow going in the opposite direction. The primary and secondary vortices are clearly visible.

In the medium-mesh computations the Reynolds number has been varied (Figure 14). For $Re_{\infty,\mathrm{SPAN}} = 10^5$ primary and secondary vortices are well resolved, while only the secondary

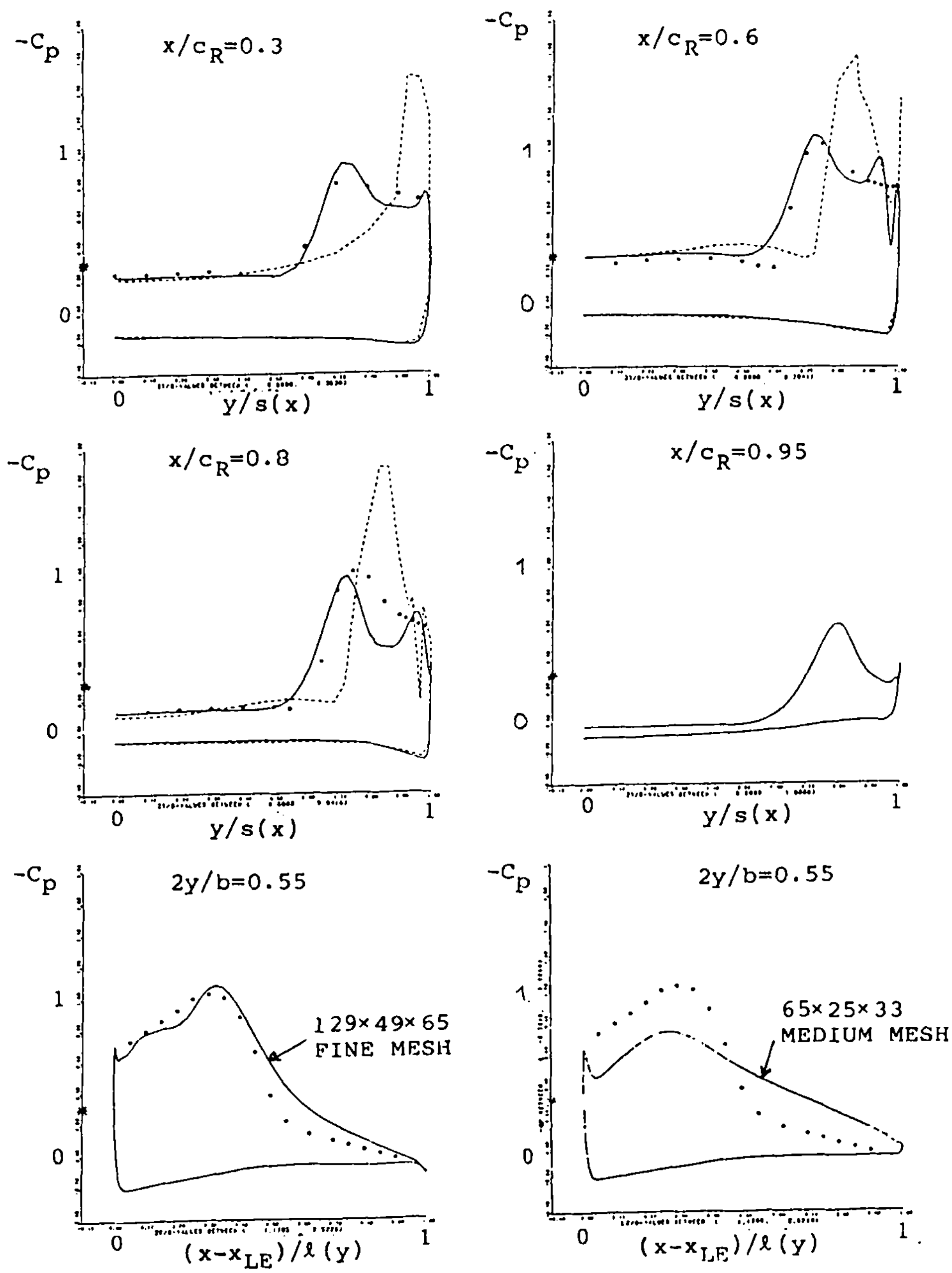

Figure 8. Comparison of pressure coefficient for $M_\infty=0{\cdot}85$, $\alpha=10^0$ and $Re_{\infty,c_R}=2{\cdot}38\times10^6$: ——, present Navier–Stokes solution; ○, experiment;[34] ---, Euler solution[35]

vortices are well represented for $Re_{\infty,\mathrm{SPAN}}=10^6$ and 10^7. Comparison of the location of the pressure minimum (not shown) and the vortex core for these Reynolds numbers shows that the primary and secondary vortices lie closer to the leading edge and tip for higher Reynolds numbers. This observation is supported by the experimental finding that the primary vortex axis moves

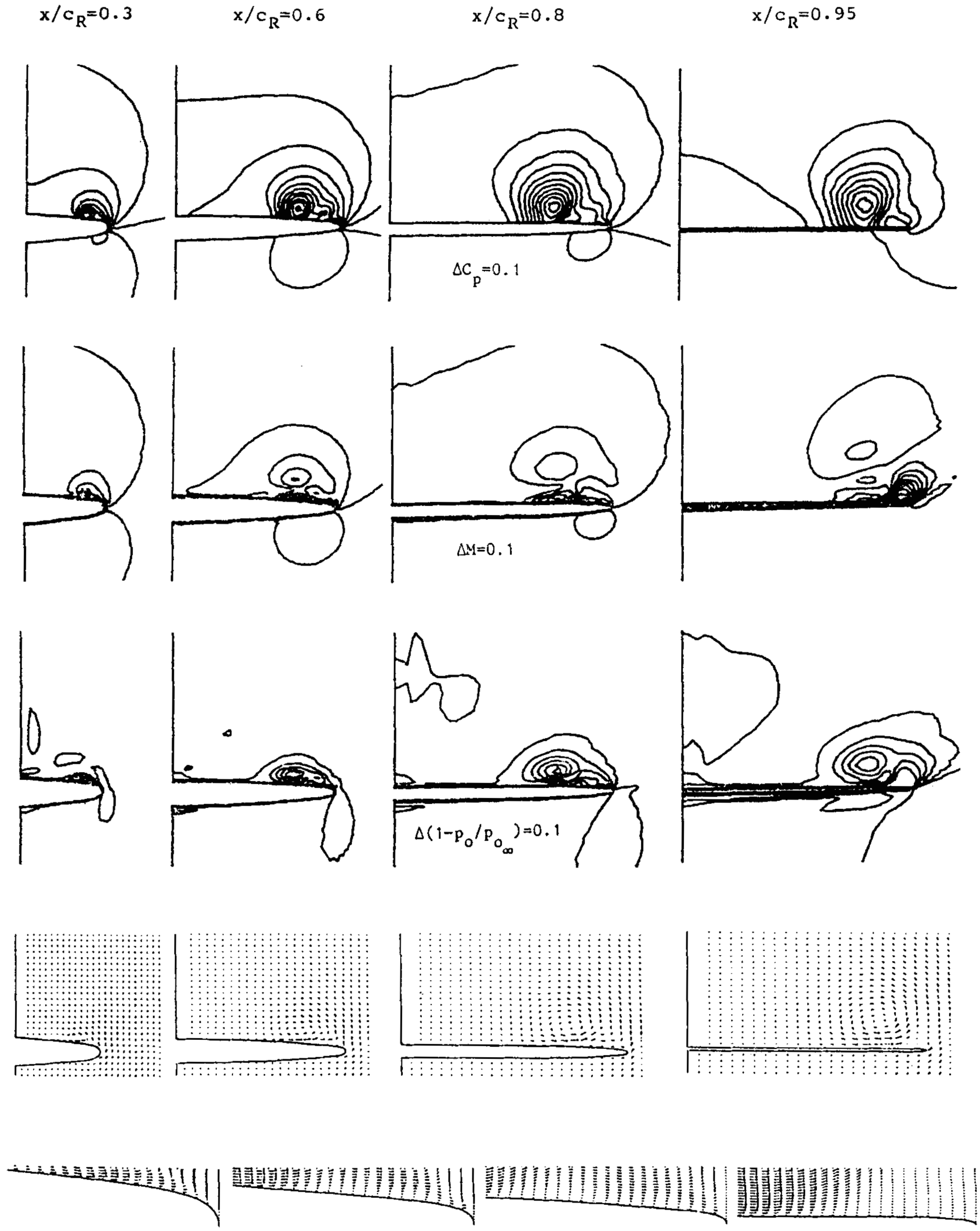

Figure 9. Pressure coefficient, Mach number and total pressure $(1-p_0/p_{0_\infty})$ contours and velocity vectors in global view and enlarged (in $2s(x)/b-0{\cdot}2 \leqslant 2y/b \leqslant 2s(x)/b$, $0 \leqslant 2z/b \leqslant 0{\cdot}05$) for $M_\infty = 0{\cdot}85$, $\alpha = 10^0$ and $Re_{\infty,c_R} = 2{\cdot}38 \times 10^6$

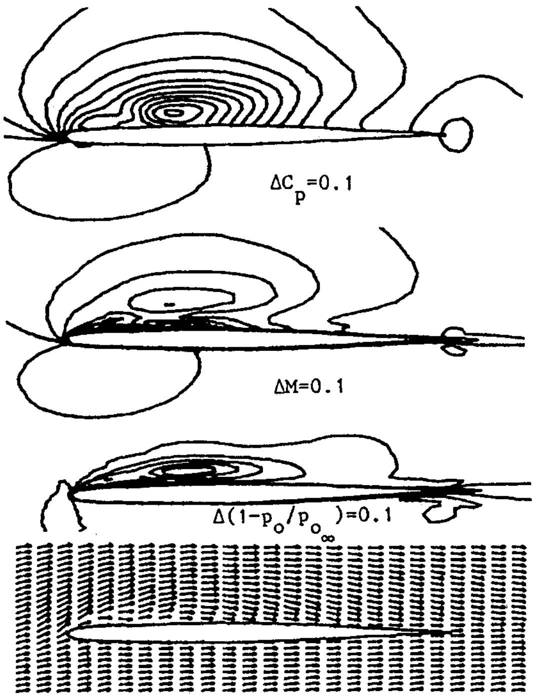

Figure 10. Pressure coefficient, Mach number and total pressure $(1-p_0/p_{0_\infty})$ contours and velocity vectors at $2s/b=0{\cdot}55$ for $M_\infty=0{\cdot}85$, $\alpha=10^0$ and $Re_{\infty,c_R}=2{\cdot}38\times10^6$

closer to the sharp leading edge of a 75° swept delta wing as the Reynolds number increases.[27] However, this effect vanishes for $Re_{\infty,c_R}>10^6$.[37]

7. CONCLUSIONS

A Navier–Stokes analysis code for laminar compressible flow over quadrilateral wings has been developed. The finite volume technique is employed with a larger difference molecule than the conventional compact differencing approach for viscous fluxes. A linear stability condition is derived to determine the local time steps and the allowable damping coefficients of the explicit Runge–Kutta scheme used for time integration. The method has been applied to simulate transonic flow over a 65° swept round leading edge cropped delta wing. The computation with a $129\times49\times65$ O–O mesh shows that the location of and pressure level under the primary vortex are predicted well compared with experimental data for $M_\infty=0{\cdot}85$, $\alpha=10°$ and $Re_{\infty,c_R}=2{\cdot}38\times10^6$. However, the pressure level between the primary and secondary vortices is overpredicted. The results obtained at $M_\infty=0{\cdot}85$, $\alpha=10^0$ and $Re_{\infty,\mathrm{SPAN}}=10^m$ $(m=5,6,7)$ indicate that the primary and secondary separation vortices lie closer to the leading edge for higher Reynolds numbers.

ACKNOWLEDGEMENTS

The authors thank Dr. G. Drougge, FFA, for valuable discussions. The extension of the second author's Euler solver to a Navier–Stokes code for quadrilateral wings was supported in part by the

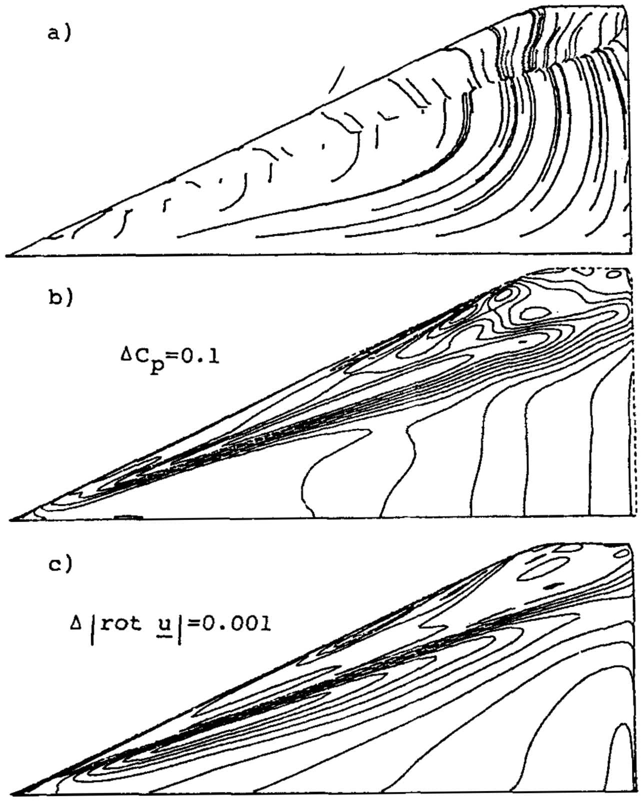

Figure 11. Skin friction lines and lines of constant C_p and |rot **u**| for $M_\infty = 0{\cdot}85$, $\alpha = 10^0$ and $Re_{\infty, c_R} = 2{\cdot}38 \times 10^6$

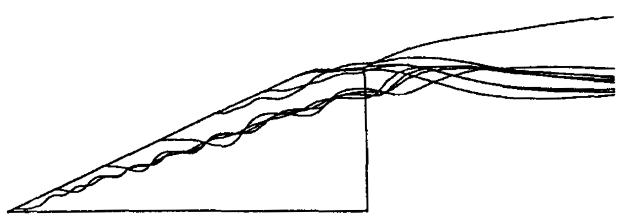

Figure 12. Streamlines on leeward side seen from above for $M_\infty = 0{\cdot}85$, $\alpha = 10^0$ and $Re_{\infty, c_R} = 2{\cdot}38 \times 10^6$

Swedish Board for Technical Development, STU, and in part by ONR during the second author's sabbatical visit at MIT. The computing time for the medium-mesh results was provided by Control Data Corporation, CDC. The fine-mesh investigation was supported in part by the Institute of Mathematics and its Applications, IMA, of the University of Minnesota, with funds provided by the National Science Foundation, NSF.

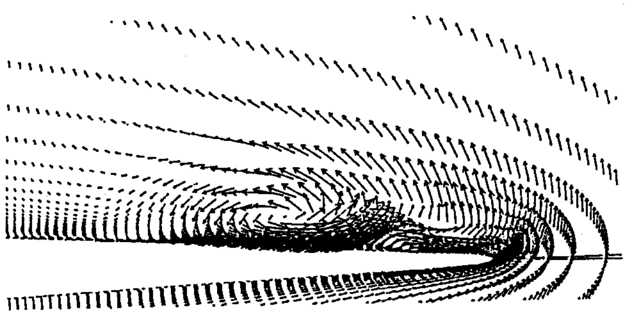

Figure 13. Velocity vectors in cells $I=33$ and 96 seen from behind for $M_\infty=0{\cdot}85$, $\alpha=10^0$ and $Re_{\infty,cR}=2{\cdot}38\times10^6$

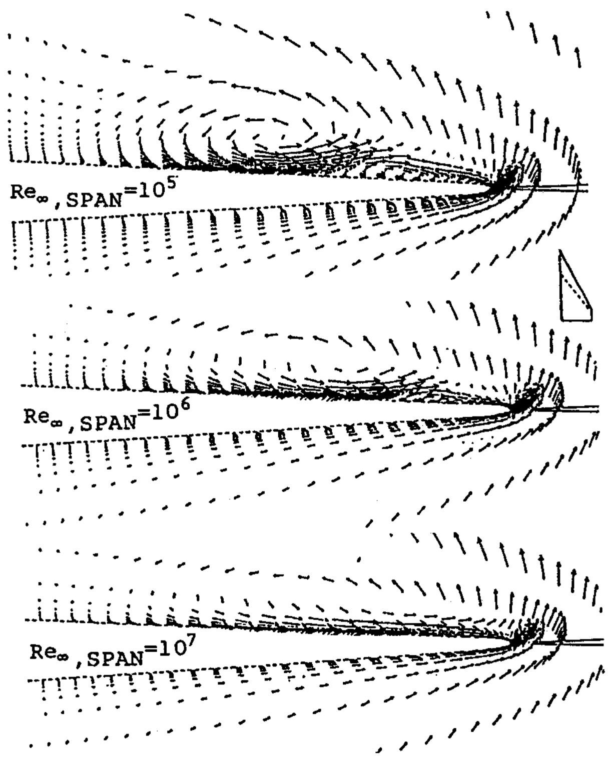

Figure 14. Velocity vectors in cells $I=17$ and 49 seen from behind for $M_\infty=0{\cdot}85$ and $\alpha=10^0$

REFERENCES

1. D. Hummel, 'Experimentelle Untersuchung dreidimensionaler laminarer Grenzschichten an einem schlanken Deltaflügel', *Z. Flugwissensch. Weltraumforsch.* **10,** (3), 133–145 (1986).
2. R. W. Newsome and O. A. Kandil, 'Vortical flow aerodynamics—physical aspects and numerical simulation', *AIAA Paper 87-0205*, January 1987.
3. R. W. MacCormack, 'The effect of viscosity in hyper-velocity impact cratering, *AIAA Paper 6-354*, 1969.
4. R. M. Beam and R. F. Warming, 'An implicit factored scheme for the compressible Navier–Stokes equations', *AIAA J.*, **16,** 393–402 (1978).

5. J. L. Thomas and R. W. Walters, 'Upwind relaxation algorithms for the Navier–Stokes equations', *AIAA Paper 85-1501 CP*, July 1985.
6. D. P. Rizzetta and J. S. Shang, 'Numerical simulation of leading edge vortex flows', *AIAA J.*, **24**, 237–245 (1986).
7. K. Fujii and P. Kutler, 'Numerical simulation of the viscous flow over three-dimensional complicated geometries', *AIAA Paper 84-1550*, June 1984.
8. J. L. Thomas, S. L. Taylor and W. K. Anderson, 'Navier–Stokes computations of vortical flows over low aspect ratio wings', *AIAA Paper 87-0207*, January 1987.
9. K. Fujii and L. B. Schiff, 'Numerical simulation of vortical flows over a strake-delta wing', *AIAA Paper 87-1229*, June 1987.
10. A. Jameson, W. Schmidt and E. Turkel, 'Numerical solutions of the Euler equations by finite volume methods using Runge–Kutta time-stepping schemes', *AIAA Paper 81-1259*, 1981.
11. A. Rizzi, 'Damped Euler-equation method to compute transonic flow around wing–body combinations', *AIAA J.*, **20**, 1321–1328 (1982).
12. W. Haase, B. Wagner and A. Jameson, 'Development of a Navier–Stokes method based on a finite volume technique for the unsteady Euler equations', in M. Pandolfi and R. Piva (eds), *Proc. 5th GAMM Conf. on Numerical Methods in Fluid Mechanics*; *Notes on Numerical Fluid Mechanics*, Vieweg, Braunschweig, 1984.
13. R. K. Agarwal and J. E. Deese, 'Computation of transonic viscous airfoil inlet, and wing flowfields', *AIAA Paper 84-1551*, 1984.
14. R. C. Swanson and E. Turkel, 'A multistage time-stepping scheme for the Navier–Stokes equations', *AIAA Paper 85-0035*, 1985.
15. L. Martinelli, E. Jameson and F. Grasso, 'A multigrid method for the Navier–Stokes equations', *AIAA Paper 86-0208*, 1986.
16. H. Reister, D. Schwamborn and H. Oertel, 'Viscous pressure wave boundary layer interaction', in Z. Youlan (ed.), *Proc. 10th Int. Conf. on Numerical Methods in Fluid Dynamics*, Springer-Verlag, New York, 1986.
17. V. Vatsa, 'Accurate solutions for transonic viscous flow over finite wings', *J. Aircraft*, **24**, 377–385 (1987).
18. D. Schwamborn, 'Simulation of the DFVLR-F5 wing experiment using a block-structured explicit Navier–Stokes method', in W. Kordulla (ed.), *Numerical Simulation of the Transonic DFVLR-F5 Wing Experiment*; *Notes on Numerical Fluid Mechanics*, Vieweg, Braunschweig, 1988.
19. R. Peyret and T. D. Taylor, *Computational Methods for Fluid Flows*, Springer-Verlag, New York, 1983.
20. A. Rizzi and L.-E. Eriksson, 'Computation of flow around wings based on the Euler equations', *J. Fluid Mech.*, **148**, 45–71 (1984).
21. W. Kordulla and M. Vinokur, 'Efficient computation of volume in flow predictions', *AIAA J.*, **21**, 917–918 (1983).
22. B. Müller and A. Rizzi, 'Runge–Kutta finite-volume simulation of laminar transonic flow over a NACA0012 airfoil using the Navier–Stokes equations', *FFA TN 1986-60*, 1986.
23. R. J. G. Norton, W. T. Thompkins and R. Haimes, 'Implicit finite difference schemes with non-simply connected grids—a novel approach', *AIAA Paper 84-0003*, January 1984.
24. L.-E. Eriksson and A. Rizzi, 'Computer-aided analysis of the convergence to steady state of discrete approximations to the Euler equations', *J. Comput. Phys.*, **57**, 90–128 (1985).
25. J. Gary, 'On certain finite-difference schemes for hyperbolic systems', *Math. Comput.*, **18**, 1–18 (1964).
26. R. W. MacCormack and B. S. Baldwin, 'A numerical method for solving the Navier–Stokes equations with application to shock–boundary layer interactions', *AIAA Paper 75-1*, January 1975.
27. S. Abarbanel and D. Gottlieb, 'Optimal time splitting for two- and three-dimensional Navier–Stokes equations with mixed derivatives', *J. Comput. Phys.*, **41**, 1–33 (1981).
28. J. Nordström, 'Stability criteria for a second order accurate, time-split finite volume scheme to solve the Navier–Stokes equation', *FFA TN 1985-08*, 1985.
29. B. Müller, 'Navier–Stokes solution for hypersonic flow over an indented nosetip', *AIAA Paper 85-1504*, July 1985.
30. L.-E. Eriksson, 'Generation of boundary conforming grids around wing–body configurations using transfinite interpolation', *AIAA J.*, **20**, 1313–1320 (1982).
31. A. Jameson and T. J. Baker, 'Solution of the Euler equations for complex configurations', *AIAA Paper 83-1929*, 1983.
32. A. Rizzi, 'Vector coding the finite-volume procedure for the CYBER 205', *Parallel Comput.*, **2**, 295–312 (1985).
33. R. H. C. Hirdes, 'US/European Vortex Flow Experiment tests report of wind tunnel measurements on the 65° wing in the NLR high speed wind tunnel HST', *NLR TR 85046 L*, 1985.
34. K. Hartmann, 'US/European Transonic Vortex Flow Experiment—data lists of pressure measurements', *DFVLR-IB 222-86 A 26*, 1986.
35. A. Rizzi, G. Drougge and C. J. Purcell, 'Euler simulation of shed vortex flows over the 65 degree delta wings', *Int. Vortex Flow Symp.*, Stockholm, 1–3 October 1986, *FFA Report*, *TN*, 1986.
36. B. Müller and A. Rizzi, 'Navier–Stokes simulation of laminar flow over the 65° round leading edge delta wing at $M_\infty = 0{\cdot}85$ and $\alpha = 10^{0}$', *Int. Vortex Flow Symp.*, Stockholm, 1–3 October 1986, *FFA Report*, *TN*, 1986.
37. R. Carcaillet, F. Manie, D. Pagan and J. L. Solignac, 'Leading edge vortex flow over a 75 degree swept delta wing: experimental and computational results', *15th ICAS Congr.*, London, 7–12 September 1986.